Monthly Notices
of the
ROYAL ASTRONOMICAL SOCIETY

MNRAS **431,** 695–709 (2013)
Advance Access publication 2013 March 04

doi:10.1093/mnras/stt201

Connecting magnetic towers with Faraday rotation gradients in active galactic nuclei jets

M. Mahmud,[1] C. P. Coughlan,[2] E. Murphy,[2] D. C. Gabuzda[2]⋆ and D. R. Hallahan[2]

[1]*Joint Institute for VLBI in Europe, Postbus 2, NL-7900 AA Dwingeloo, the Netherlands*
[2]*Physics Department, University College Cork, Cork, Ireland*

Accepted 2013 January 31. Received 2013 January 31; in original form 2011 September 8

ABSTRACT

The idea that systematic Faraday Rotation gradients across the parsec-scale jets of active galactic nuclei (AGNs) can reveal the presence of helical magnetic (***B***) fields has been around since the early 1990s, although the first observation of this phenomenon was about ten years later. These gradients are taken to be due to the systematic variation of the line-of-sight ***B*** field across the jet. We present here, the parsec-scale Faraday Rotation distributions for the BL Lac objects 0716+714 and 1749+701, based on polarization data obtained with the Very Long Baseline Array at two wavelengths near each of the 2 cm, 4 cm and 6 cm bands (0716+714) and at four wavelengths in the range 18–22 cm (1749+701). The Rotation Measure (RM) maps for both these sources indicate systematic gradients across their jets, as expected if these jets have helical ***B*** fields. The significance of these transverse RM gradients is $>3\sigma$ in all cases. We present the results of Monte Carlo simulations directly demonstrating the possibility of observing such transverse RM gradients even if the intrinsic jet structure is much narrower than the observing beam. We observe an intriguing new feature in these sources, a reversal in the direction of the gradient in the jet as compared to the gradient in the core region. This provides new evidence to support models in which field lines emerging from the central region of the accretion disc and closing in the outer region of the accretion disc are both 'wound up' by the differential rotation of the disc. The net observed RM gradient will essentially be the sum effect of two regions of helical field, one nested inside the other. The direction of the net RM gradient will be determined by whether the inner or outer helix dominates the RM integrated through the jet, and RM gradient reversals will be observed if the inner and outer helical fields dominate in different regions of the jet. This potentially provides new insights about the overall configuration of the jet ***B*** fields.

Key words: galaxies: active – galaxies: magnetic fields – galaxies: jets – BL Lacertae objects: individual: 0716+714 – BL Lacertae objects: individual: 1749+701.

1 INTRODUCTION

The radio emission of Active Galactic Nuclei (AGNs) is synchrotron radiation generated in the relativistic jets that emerge from the nucleus of the galaxy, presumably along the rotational axis of a central supermassive black hole. Synchrotron radiation can be highly linearly polarized, up to $\simeq$75 per cent in the case of a uniform magnetic (***B***) field (Pacholczyk 1970). Linear polarization observations are essential, as they give information about the orientation and degree of the order of the ***B*** field, as well as the distribution of thermal electrons and the ***B***-field geometry in the vicinity of the AGN. Many theorists have suggested that the magnetic fields of these sources are closely connected with the collimation of the jets, and could determine whether sources have prominent jets or not (e.g. Meier, Koide & Uchida 2001). Thus, information on the magnetic fields of these sources is essential in helping us better understand various physical processes in AGN jets.

Very long baseline interferometry (VLBI) polarization observations of BL Lac objects have shown a tendency for the polarization ***E*** vectors in the parsec-scale jets to be aligned with the local jet direction, which implies that the corresponding ***B*** field is transverse to the jet, because the jet is optically thin (Gabuzda, Pushkarev & Cawthorne 2000). It seems likely that many of these transverse ***B*** fields represent the ordered toroidal component of the intrinsic ***B*** fields of the jets, as discussed by Gabuzda et al. (2008), see also references therein. Depending on the observer's viewing angle and the helix's pitch angle, helical jet ***B*** fields can also give rise to a 'spine-sheath' polarization structure in the frame of the observer, with a region of longitudinal polarization (transverse ***B*** vectors) along the

⋆ E-mail: d.gabuzda@ucc.ie (DCG)

central 'spine' of the jet surrounded by regions of transverse polarization (longitudinal $\boldsymbol{B}$ vectors) near the edges of the jet. The presence of transverse polarization near the edges of the jet could be a natural consequence of a helical jet $\boldsymbol{B}$ field, although it has also been suggested to be due to interaction with the surrounding medium (Laing 1996; Attridge, Roberts & Wardle 1999; Lyutikov, Pariev & Gabuzda 2005; Pushkarev et al. 2005).

Faraday Rotation studies can play a key role in determining the intrinsic $\boldsymbol{B}$-field geometries associated with the jets. Faraday Rotation of the plane of linear polarization occurs during the passage of an electromagnetic wave through a region with free electrons and a magnetic field with a non-zero component along the line of sight. The amount of rotation is proportional to the integral of the density of free electrons n_e multiplied by the line-of-sight $\boldsymbol{B}$ field, the square of the observing wavelength λ^2 and various physical constants; the coefficient of λ^2 is called the Rotation Measure (RM):

$$\Delta\chi \propto \lambda^2 \int n_e B \cdot \mathrm{d}l \equiv \mathrm{RM}\lambda^2. \quad (1)$$

The intrinsic polarization angle can be obtained from the relation:

$$\chi_{\mathrm{obs}} = \chi_0 + \mathrm{RM}\lambda^2, \quad (2)$$

where χ_{obs} is the observed polarization angle, χ_0 is the intrinsic polarization angle in the absence of Faraday rotation and λ is the observing wavelength. Simultaneous multifrequency observations thus potentially enable the determination of the RM, as well as identification of the intrinsic polarization angles.

Systematic gradients in the Faraday RM have been reported previously across the parsec-scale jets of several AGNs, interpreted as reflecting the systematic change in the line-of-sight component of a toroidal or helical jet $\boldsymbol{B}$ field across the jet (Blandford 1993; Asada et al. 2002; Gabuzda, Murray & Cronin 2004; Zavala & Taylor 2005; Gabuzda et al. 2008; Asada et al. 2008a,b, 2010; Mahmud, Gabuzda & Bezrukovs 2009). Such fields would come about in a natural way as a result of the 'winding up' of an initial 'seed' field by the differential rotation of the central accreting objects (e.g. Nakamura, Uchida & Hirose 2001; Lovelace et al. 2002).

We consider here two objects in which we have detected transverse RM gradients in both the core region and jet: 0716+714 and 1749+701. In both cases, there is a reversal of the direction of the RM gradient between these two regions. We discuss a possible explanation of this phenomena based on magnetic-tower-type models for jet launching. Throughout, we assume $H_0 = 71$ km s^{-1} Mpc^{-1}, $\Omega_\lambda = 0.73$ and $\Omega_m = 0.27$.

2 FARADAY ROTATION OBSERVATIONS AND REDUCTION

Very Long Baseline Array (VLBA) polarization observations of the sources included in this paper were carried out as part of two different studies of the same sample of BL Lac objects: one at 4.6–15.4 GHz and one at 1.36–1.67 GHz. The high-frequency observations of 0716+714 were on 2004 March 22 and of 1749+701 were on 2003 August 22; the low-frequency observations of 1749+701 were on 2004 January 17. In both cases, the distributions of u–v points were virtually identical for the different frequencies observed during a single set of observations, with the baseline lengths scaled in accordance with the individual observing frequencies.

Standard tasks in the National Radio Astronomy Observatory (NRAO) AIPS package were used for the amplitude calibration and preliminary phase calibration. The instrumental polarizations ('D-Terms') were determined with the task 'LPCAL', solving simultaneously for the source polarization. In all cases, the reference antenna used was Los Alamos.

The Electric Vector Position Angle (EVPA) calibration was done using integrated polarization observations of bright, compact sources, obtained with the Very Large Array (VLA) near in time to our VLBA observations, by rotating the EVPA for the total VLBI polarization of the source to match the EVPA for the integrated polarization of that source derived from VLA observations.

2.1 2003 August and 2004 March observations: 4.6–15.4 GHz

The observations were carried out at six frequencies: 4.612, 5.092, 7.916, 8.883, 12.939 and 15.383 GHz. Each source was observed for about 25–30 min at each frequency, in a 'snap-shot' mode with 8–10 scans spread out over the observing time period. Presented in this paper are the results for 0716+714 (observed on 2004 March 22) and 1749+701 (observed on 2003 August 22).

The instrumental polarizations ('D-Terms') were determined using observations of 1156+295 (2003 August 22) and 0235+164 (2004 March 22). The source of the integrated VLA polarizations for the EVPA calibration was the NRAO website (www.aoc.nrao.edu/smyers/calibration/). The VLA observations were made at frequencies 5, 8.5, 22 and 43 GHz. We found these EVPA values to be consistent with a linear λ^2 law (Faraday Rotation) and were thus able to interpolate the corresponding values for our non-standard frequencies (see Mahmud et al. 2009). The sources used were 1803+784 and 2200+420. We refined our initial EVPA calibration by examining the resulting polarization images for several sources with simple structures and checking for consistency. This led to adjustments of 5–20° for several of the EVPA corrections. This procedure improved the overall self-consistency of the polarization and RM maps for virtually all of the sources observed. We estimate that our overall EVPA calibration is accurate to within 3°. A summary of our final 4.6–15.4 GHz EVPA corrections is given in Mahmud et al. (2009).

To verify the accuracy of the overall flux calibration at 4.6–15.4 GHz, we determined the spectra of various optically thin regions in the jet of 1803+784, after taking into account the relative shifts between the images (see Mahmud et al. 2009). The observed 4.6–15.4 GHz fluxes are consistent with a power law within the errors, corresponding to a 'normal' optically thin spectral indices of $\simeq$1.

2.2 2004 January observations: 1.36–1.67 GHz

Results for 1749+701 at epoch 2004 January 17 at four frequencies between 1.358 and 1.665 GHz are also included in this paper. The instrumental polarizations ('D-Terms') for these observations were determined using observations of 0851+202. The absolute calibration of the EVPAs was determined using VLA observations of 0851+202 obtained at 1.485 and 1.665 GHz on 2004 February 20. These observations were sufficiently close in time to the VLBA observations to be suitable for the EVPA calibration because the polarization is not rapidly variable at such low frequencies. A lambda-squared fit was applied to the VLA polarization angles, yielding an RM of +31.6 rad m^{-2}, in excellent agreement with the previously measured value of +31 ± 2 (Pushkarev 2001). We accordingly used the measured VLA polarization angles and RM to determine the integrated polarization angles for our four VLBA frequencies, which were then used to calibrate the VLBA EVPAs. We estimate the errors in the resulting polarization angles to be no more than 2°. For a list of the observing frequencies and their EVPA corrections, see Table 1.

Table 1. EVPA calibrations for 2004 January 17.

Frequency (GHz)	$\Delta\chi$ (deg)
1.358	128.1
1.430	111.1
1.493	100.4
1.665	82.5

2.3 Rotation measure determination

We made maps of the distribution of the total intensity I and Stokes parameters Q and U at each of the frequencies, with matched cell sizes, images sizes and resolutions, by convolving all of the final maps with the same beam. The distributions of the polarized flux ($p = \sqrt{Q^2 + U^2}$), as well as maps of the EVPA ($\chi = \frac{1}{2}\arctan\frac{U}{Q}$) and χ noise maps, were obtained from the Q and U maps using the task 'COMB'.

Although the Q and U maps at each frequency will be properly aligned with the I map at that same frequency, the images at different frequencies can be appreciably shifted relative to each other. The physical origin of this effect is the fact that the mapping procedure effectively aligns the images roughly on the bright, compact VLBI core, whose position depends on the observing frequency: the core ($\tau = 1$ surface) appears further down the jet at lower frequencies (Königl 1981). It is important to correct for this effect by properly aligning the I images before making spectral-index maps; although the effect of modest misalignments between the χ maps at different frequencies is much smaller, it is nevertheless optimal to align these maps before constructing RM maps to maximize the reliability of the resulting RM maps.

We determined the relative shifts between the maps at each of our frequencies using the cross-correlation algorithm of Croke & Gabuzda (2008), which essentially aligns the images based on their optically thin jet emission. This procedure yielded only negligible 'core-shifts' for 0716+714 in our frequency range (less than a pixel), consistent with the results of Kovalev et al. (2008). The core-shift for 1749+701 between 4.6 and 15.4 GHz is appreciable: approximately 0.8 mas in position angle -63°, aligned with the VLBI jet direction. The shifts between the other frequencies and 15.4 GHz were smaller and consistent with the expected scaling with frequency. We accordingly used these shifts to align the polarization-angle maps for 1749+701 before making the high-frequency RM map. We verified that the shifts between the images at the lower frequencies (1.36–1.67 GHz) were negligible for all sources observed in that experiment, including 1749+701; this is expected, since these frequencies do not cover a wide range; accordingly, no shifts were necessary for those images.

Furthermore, we constructed maps of the RM, using the AIPS task 'RM', after first subtracting the effect of the integrated RM (Pushkarev 2001), presumed to arise in our Galaxy, from the observed polarization angles, so that any residual Faraday Rotation was due to only the thermal plasma in the vicinity of the AGN. We used a modified version of 'RM' enabling simultaneously RM fitting using up to eight frequencies. We used the option in the task 'RM' of blanking output pixels when the uncertainty in the RM exceeds a specified value, which was about 30 rad m^{-2} for the high-frequency maps and about 10 rad m^{-2} for the low-frequency maps. This uncertainty in the RM calculated for a given pixel by the 'RM' task is based on a fit of χ versus λ^2 weighted by the uncertainties in the polarization angles, which are, in turn, calculated using the noise levels on the Stokes Q and U maps. Thus, the resulting RM uncertainties for individual pixels are determined both by the uncertainties in the polarization angles and the quality of the linear λ^2 fit. The blanking levels we chose were determined empirically, as the maximum values that did not lead to any obviously spurious features in the RM maps, either at the location of the source or in the rest of the map. The blanking applied essentially means that the output RM values show some evidence of reality and reliability – collocation with the source emission region and agreement with a λ^2 law within the specified limit.

3 ESTIMATION OF THE χ AND RM UNCERTAINTIES

It has been usual to adopt the root-mean-square (rms) deviations in the residual map (or in the final CLEAN map far from any regions containing real flux) $\sigma_{\rm rms}$ as an estimate of the total uncertainty in the measured flux in an individual pixel. Hovatta et al. (2012) have recently investigated this practice empirically using Monte Carlo simulations. They concluded that the uncertainties in Q and U fluxes in individual pixels are described well by the expression

$$\sigma = \sqrt{\sigma_{\rm rms}^2 + \sigma_{\rm Dterm}^2 + (1.5\sigma_{\rm rms})^2}, \quad (3)$$

where $\sigma_{\rm Dterm}$ is associated with the presence of residual instrumental polarizations in the data (see also Roberts, Wardle & Brown 1994):

$$\sigma_{\rm Dterm} \simeq \frac{\sigma_\Delta}{\sqrt{N_{\rm ant} N_{\rm IF} N_{\rm scan}}} \sqrt{I^2 + (0.3\, I_{\rm peak})^2}, \quad (4)$$

where σ_Δ is the estimated uncertainty in the individual D-terms, $N_{\rm ant}$ the number of antennas in the VLB array (assuming all have altitude-azimuth mounts), $N_{\rm IF}$ the number of IFs (sub-bands within the total observed band at a given frequency) used for the observations, $N_{\rm scan}$ the number of scans with independent parallactic angles, I the total intensity at the point in question, and $I_{\rm peak}$ the total intensity at the map peak. The term containing $I_{\rm peak}$ was added by Hovatta et al. (2012) to approximately take into account the fact that the residual D-term uncertainty tends to scatter polarized flux throughout the map. The expression for σ above explicitly demonstrates that, even if the D-term error term is negligible, the uncertainty in fluxes in regions of source emission is somewhat higher than the map rms in regions far from source emission.

In our case, $N_{\rm ant} = 10$, $N_{\rm IF} = 4$ for the 7.9–15.4 GHz observations and 2 for the 4.6 GHz, 5.1 GHz and 1.36–1.67 GHz observations, and $N_{\rm scan} \simeq 8$. We estimate $\sigma_\Delta \simeq 0.005$ for all the experiments from the scatter in the D-terms. The largest value for $\sigma_{\rm Dterm}$ will occur at the peaks of the maps; at the positions where we have determined the RM values below (Table 2), the resulting D-term uncertainties are no more than $\simeq 0.60\sigma_{\rm rms}$ for 0716+714 and no more than $\simeq 0.40\sigma_{\rm rms}$ for 1749+701, making $\sigma_{\rm Dterm}$ small compared to the other terms contributing to σ.

The Q and U uncertainties determined in this way can then be propagated to derive the corresponding uncertainties in the polarization angles, σ_χ:

$$\chi = \frac{1}{2}\arctan\left(\frac{U}{Q}\right) \quad (5)$$

$$\sigma_\chi^2 = \frac{1}{4}\left[\left(\frac{Q}{Q^2+U^2}\right)^2 \sigma_U^2 + \left(\frac{U}{Q^2+U^2}\right)^2 \sigma_Q^2\right] \quad (6)$$

The uncertainty in the EVPA calibration $\sigma_{\rm EVPA}$ can then be added in quadrature:

$$\sigma_{\chi_{\rm final}}^2 = \sigma_\chi^2 + \sigma_{\rm EVPA}^2. \quad (7)$$

Table 2. RM measurements in Figs 5 and 6.

Figure	Source	Point in plot	Position (mas)	RM rad m^{-2}	Left–Right RM difference	RM difference in σ
(1)	(2)	(3)	(4)	(5)	(6)	(7)
5 (left)	0716+714	Left	(+0.90, −1.00)	−256 ± 53		
	(Core-region)	Mid	(0.10, −0.80)	−41 ± 44	+262 ± 60	4.4σ
		Right	(−0.70, −0.60)	+6 ± 28		
5 (right)	0716+714	Left	(+1.00, +1.00)	+94 ± 37		
	(Jet)	Mid	(+0.30, +1.00)	−31 ± 9	−239 ± 47	5.1σ
		Right	(−0.50, +1.10)	−145 ± 29		
6 (left)	1749+701	Left	(+9.00, +1.50)	−19 ± 8		
	(Core-region)	Middle	(+4.50, −3.00)	+13 ± 4	+39 ± 9	4.3σ
		Right	(−1.50, −7.50)	+20 ± 2		
6 (right)	1749+701	Left	(−4.50, +9.00)	+17 ± 10		
	(Jet)	Middle	(−6.00, +3.00)	+4 ± 6	−38 ± 12	3.2σ
		Right	(−7.50, −3.00)	−21 ± 6		

These χ uncertainties can then, in turn, be used to determine uncertainties in the fitted RM values, as is described by Hovatta et al. (2012).

Note, however, that as the same EVPA calibration is applied to each polarization angle at a given frequency, the uncertainty this introduces is *systematic*. One consequence of this is that, although the EVPA calibration uncertainties will increase the uncertainties in the fitted RM values, EVPA calibration uncertainties should not give rise to spurious RM gradients (e.g. Mahmud et al. 2009; Hovatta et al. 2012). The reason for this is essentially that any EVPA calibration error corresponds to a specific systematic offset that affects all EVPA measurements at all points of the maps at the corresponding frequency equally *and in the same direction*, and so will not induce gradients between points.

This was taken into account in our analysis in the same way as was done by Mahmud et al. (2009) and Hovatta et al. (2012): when RM values are derived specifically so that they can be compared to search for possible gradients, the value σ_χ without adding $\sigma_{\rm EVPA}$ in quadrature was used to determine the RM uncertainty.

4 RESULTS

The images in Fig. 1 show the observed VLBI total-intensity and linear-polarization structures for both sources at 15.4, 7.9 and 4.9 GHz, and Fig. 2 the total-intensity and linear-polarization structure of 1749+701 at 1.43 GHz, all corrected for integrated but not local Faraday Rotation. The maps at 1.36, 1.49 and 1.67 GHz are very similar, and are not shown here. The convolving beams used in each case are indicated in the lower right-hand corner of the figures. The peaks and bottom contours are indicated in the figure captions and, in all cases, the contour levels increase in steps of a factor of 2.

0716+714 has a redshift of $z = 0.30$, corresponding to 4.52 pc mas^{-1}, and an integrated RM of −30 rad m^{-2} (Pushkarev 2001). The jet of 0716+714 extends roughly to the north. The jet polarization $\boldsymbol{E}$ vectors are aligned with the local jet direction, as is also shown by the 2 cm MOJAVE images (http://www.physics.purdue.edu/MOJAVE/sourcepages/).

1749+701 has a redshift of $z = 0.77$, corresponding to 7.41 pc mas^{-1}, and an integrated RM of +15 rad m^{-2} (Pushkarev 2001). The jet of 1749+701 initially emerges towards the northwest, then turns towards the north and further towards the east; this spiral-like path is evident in the 7.9 and 4.9 GHz maps (see also Gabuzda & Lisakov 2009). The polarization $\boldsymbol{E}$ vectors are mostly aligned with the local jet direction; some regions of 'spine-sheath' polarization structure or orthogonal polarization offset towards one side of the jet are visible in the maps. Although the core–jet structure is not directly distinguishable in the 1.43 GHz image for 2004 January in Fig. 2, the orientation of this structure is known from the higher frequency images in Fig. 1. The polarization $\boldsymbol{E}$ vectors appear to be aligned with the jet direction. The weak emission to the southeast of the map centre corresponds to a continuation of the emission in roughly this region in the 4.9 GHz image (Fig. 1, bottom right).

The images in Figs 3 and 4 show the parsec-scale RM distributions for 0716+714 (4.6–15.4 GHz) and 1749+701 (1.36–1.67 GHz), superimposed on the corresponding I contours. The RM distribution for 1749+701 for 4.6–15.4 GHz is subject to uncertainty due to the relatively large shifts required to align the χ images at the different frequencies, and we accordingly focus on the more reliable images shown in these two figures. In all cases, the I contours increase in steps of a factor of 2. The arrows show the direction of RM gradients in the corresponding regions visible by eye; in other words, the direction in which the value of the RM increases (from more negative to less negative, negative to positive or less positive to more positive, as the case may be). The convolving beams used in each case are indicated in the lower right-hand corner of the figures. The beam used for the 4.6–15.4 GHz RM map for 0716+714 was 1.28 mas × 1.06 mas in position angle −0.°84, which corresponds to the resolution of the 7.9 GHz data; this beam was chosen in order to provide slightly higher resolution in the RM map at the expense of only a modest overresolution of the lowest frequency images. Accompanying panels show plots of polarization angle (χ) versus wavelength squared (λ^2) for the indicated regions; the uncertainties in the polarization angles shown here include the EVPA uncertainty added in quadrature. Slices of the RM across the gradients in the specified locations in the jets and core regions obtained with the AIPS task 'SLICE' are also shown; we do not include the (single-pixel-based) uncertainties on these slices on these plots, since they are meant only to be orientational. Instead, we carry out below an analysis involving the RM values and their uncertainties for three regions across the jet (on either side and in the centre), more in keeping with the limited resolution available with our arrays.

5 DISCUSSION

5.1 Linear polarization structure

Previous polarization observations have demonstrated that 'spine-sheath' polarization structures are not uncommon among blazars.

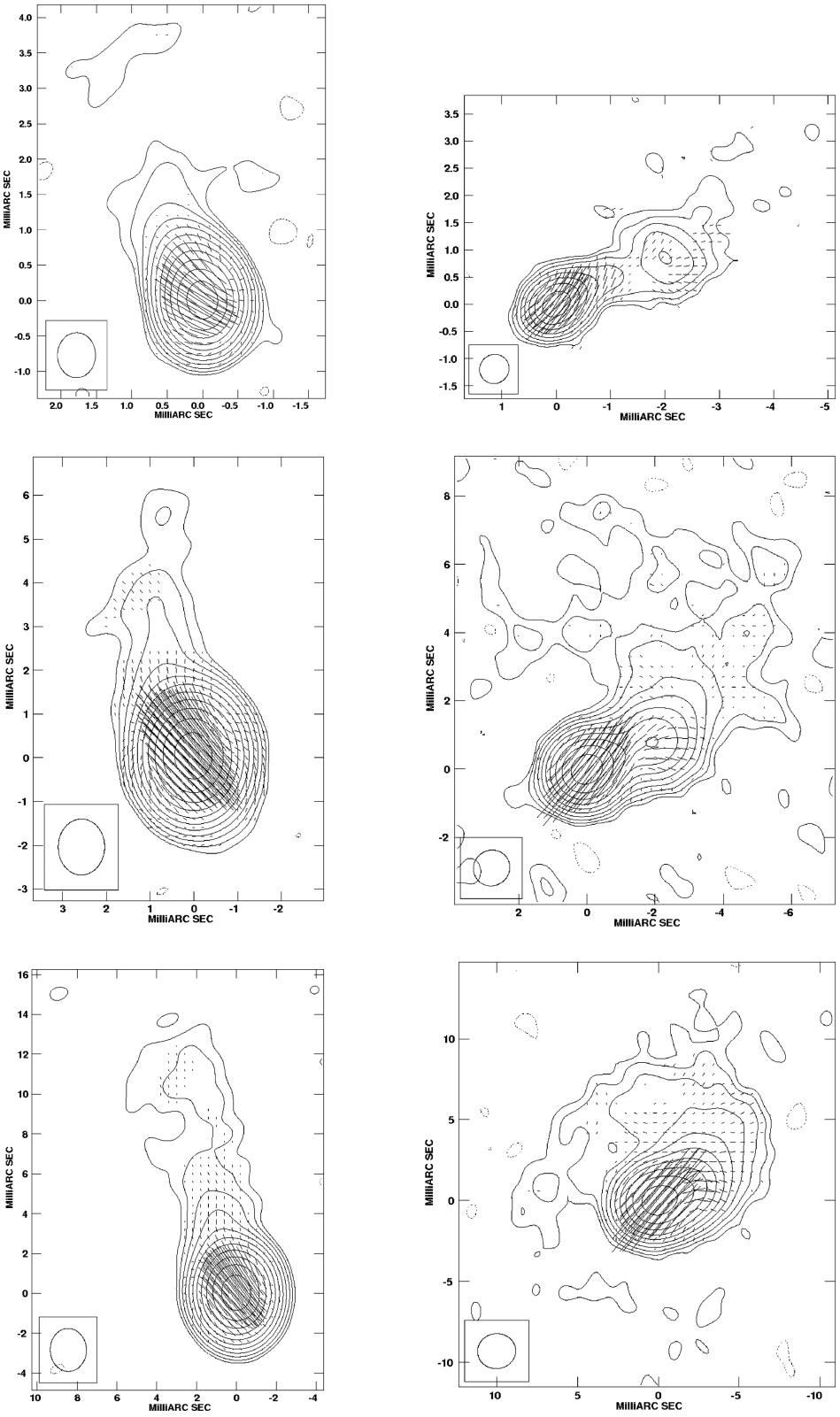

Figure 1. VLBA *I* maps for 0716+714 (left) and 1749+701 (right) with polarization sticks superimposed, at 15.4 GHz (top), 7.9 GHz (middle) and 4.6 GHz (bottom), corrected for integrated Faraday Rotation. The maps of 0716+714 have peaks of 1.0, 1.3 and 1.5 Jy beam^{-1} and bottom contours of 0.7, 0.8 and 0.9 mJy beam^{-1}; the maps of 1749+701 have peaks of 0.5, 0.4 and 0.3 Jy beam^{-1} and bottom contours of 0.6m, 0.5 and 1.7 mJy beam^{-1}.

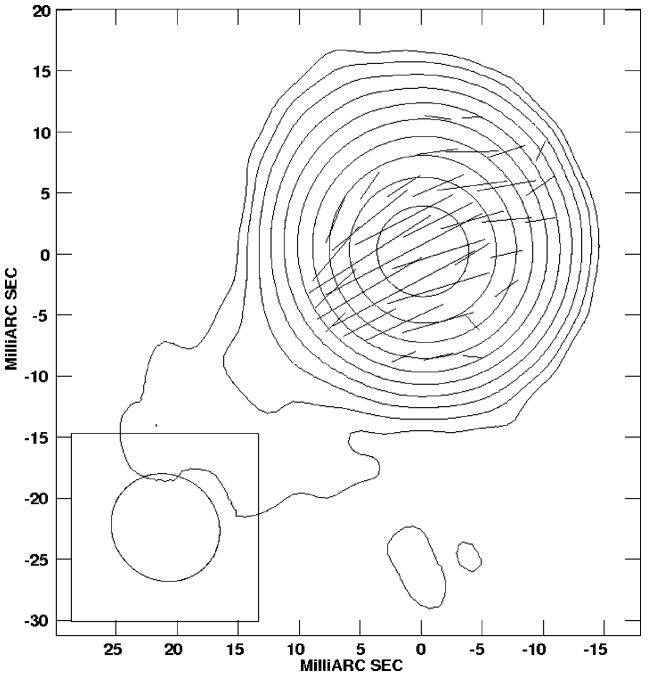

Figure 2. VLBA *I* map of 1749+701 with polarization sticks superimposed, at 1.43 GHz, corrected for integrated Faraday Rotation. The *I* peak is 0.60 Jy beam^{-1} and the bottom contour is 1.5 mJy beam^{-1}.

Attridge et al. (1999) interpreted a 'spine-sheath' polarization structure in the jet of the quasar 1055+018 as a result of a series of shocks compressing the field in the central region and shearing of the field induced by interaction with the surrounding medium at the jet edges. However, more recent studies (e.g. Lyutikov et al. 2005; Pushkarev et al. 2005) have discussed the possibility that 'spine-sheath' polarization structures can come about naturally in the case of helical jet magnetic fields. The BL Lac objects 0714+716 and 1749+701 both show signs of 'spine-sheath' polarization or transverse polarization offset towards one side of the jet at one or more wavelengths, consistent with the possibility that their jets carry helical magnetic fields.

5.2 Detection of transverse RM gradients across the jets

Tentative transverse RM gradients across the jets of the two BL Lac objects considered here are visible by eye in the colour versions of the RM distributions in Figs 3 and 4. The first step in testing the reality of these gradients is estimating the uncertainties in the RM values on either end of the gradient, to determine at what level the two RM values differ. We have done this using the Q and U uncertainty relations of Hovatta et al. (2012), as described above.

Figs 5 and 6 show plots of the observed RMs at three points across the core-region and jet structures of 0716+714 and 1749+701 (on either side and near the centre). Together with the slices shows in Figs 3 and 4, these figures demonstrate the systematic, monotonic nature of these observed RM gradients.

Table 2 summarizes the sets of RM values shown in Figs 5 and 6 together with their uncertainties, as well as the differences between the RM values on either side of the inferred transverse gradients and their uncertainties. The columns present (1) the figure to which the RM values refer, (2) the source name, (3) the point in the indicated figure to which the RM value corresponds, (4) the position where the RM value was measured, in milliarcseconds, relative to the phase centre, (5) the RM value at the indicated position, together with its uncertainty, (6) the difference between the two RM values on either side of the source structure and its uncertainty and (7) the significance of this difference in numbers of σ. The uncertainties listed in column (5) are based on χ uncertainties without the EVPA-calibration uncertainty added in quadrature, since this will affect all points in an RM image systematically in the same way. The last column of this table shows that the differences between the RM values detected on either side of the jet structures are at the level of 3–5σ, demonstrating that these differences appear to be statistically significant.

5.3 The possibility of detecting transverse RM gradients across narrow jets

Taylor & Zavala (2010) have recently proposed four criteria for the reliable detection of transverse Faraday Rotation gradients, the most stringent of which is that the observed RM gradient span at least three 'resolution elements' across the jet. This criterion reflects the desire to ensure that it is possible to distinguish properties between regions located on opposite sides of the jets. The criterion of three 'resolution elements' has been taken to correspond to three beamwidths, and coincides with the general idea that structures separated by less than a beamwidth are not well resolved.

To test the validity of this criterion of Taylor & Zavala (2010), we constructed core–jet-like sources with various intrinsic widths and with transverse RM gradients present across their structures and carried out Monte Carlo simulations based on these model sources. A description of our Monte Carlo simulations and the results they yielded are presented in the Appendix. The transverse source widths for our model sources correspond to intrinsic widths of about 1/2, 1/3, 1/5, 1/10 and 1/20 of the beam full width at half-maximum (FWHM) in the direction across the jet. The simulations show that the transverse RM gradients introduced into the model visibility data remain visible in the RM maps constructed from 'noisy' data having the same distribution of (u, v) points as our observations of 0716+714, even when the intrinsic width of the structure is much smaller than the beam width. Both unidirectional model RM gradients and model RM structure containing two oppositely directly transverse gradients in the core region and jet are visible for all the jet widths considered.

The results of these new Monte Carlo simulations thus directly demonstrate that the three-beamwidth criterion of Taylor & Zavala (2010) is overly restrictive, since the simulations directly show the possibility of detecting transverse RM gradients even when the intrinsic widths of the corresponding source structures are much less than the beamwidth, resulting in RM distributions that span only 1–1.5 beamwidths. This demonstrates that the relatively modest widths spanned by the transverse RM gradients in 0716+714 and 1749+701 that we report here should not be taken by themselves as grounds to question the reliability of these gradients. We note here that our Monte Carlo simulations are not intended to provide a physical model for our observations, or to reproduce our observed RM distributions in any detail; instead, they are intended solely to demonstrate the possibility of detecting a transverse RM gradient in real data, even if the intrinsic jet width is much smaller than the beam FWHM.

Inspection of fig. 30 of Hovatta et al. (2012) indicates that the fraction of 'false positives', i.e. spurious RM gradients, that were obtained in their Monte Carlo simulations did not exceed $\simeq$1 per cent when a 3σ criterion was imposed for the RM gradient, even when the observed width of the RM gradient was less than 1.5 beamwidths.

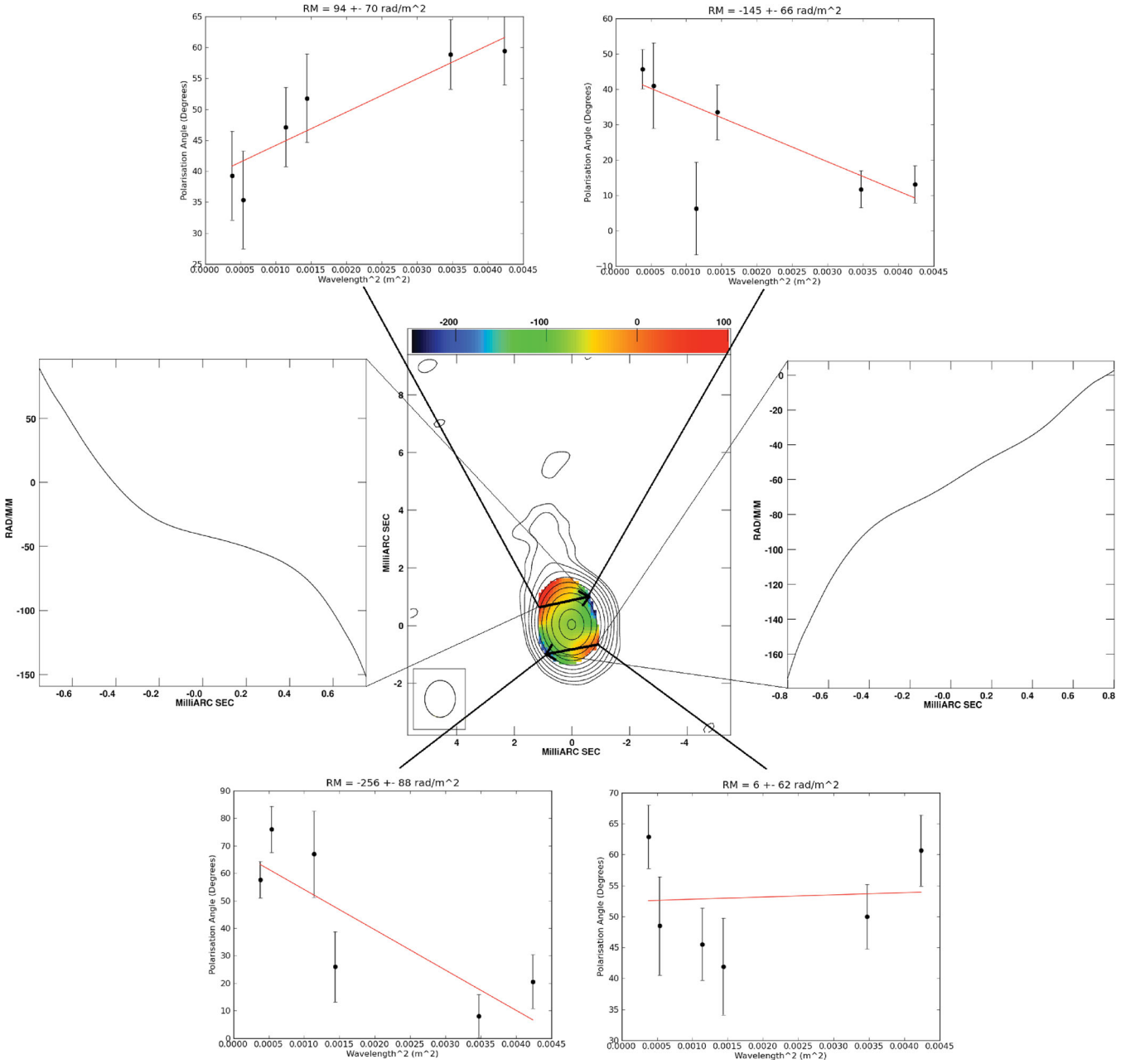

Figure 3. RM map of 0716+714 at 4.6–15.4 GHz. The accompanying panels show slices of the RM distributions across the jet and core, and polarization angle (χ) versus wavelength-squared (λ^2) plots for pixels on either side of the core and jet. The errors shown in the plots are 1σ, and include the estimated random errors and the EVPA uncertainties added in quadrature. The peak of the I map is 1.3 Jy beam^{-1} and the bottom contour is 1.0 mJy beam^{-1}. The beam used to construct the I and RM maps was 1.28 × 1.06 mas in position angle $-0\overset{\circ}{.}8$.

This suggests that there may be up to a $\simeq$1 per cent probability that the RM gradients we report here are spurious, due to their relatively limited widths, although we consider this to be unlikely, given that the RM differences involved correspond to as much as 5σ.

5.4 The remaining criteria of Taylor & Zavala (2010)

With regard to the other criteria for reliability of transverse RM gradients proposed by Taylor & Zavala (2010), the criterion that the change in the RM across the jet be at least 3σ is satisfied by the RM images in Figs 3 and 4 (see also Table 2). The differences in the RMs across the core region and jet of 0716+714 (Fig. 5) are approximately 4–5σ; the differences in the RMs across the core region and jet of 1749+701 (Fig. 6) are approximately 3–4σ.

The criterion that the change in the RM be monotonic and smooth within the errors is also satisfied by the gradients in both 0716+714 and in 1749+701. Although the gradients suggested by the slices displayed in Figs 3 and 4 are not constant (linear), they are nevertheless monotonic. It is interesting to note here that the simulated RM maps of Broderick & McKinney (2010) typically do not show RM gradients with a constant slope all across the RM distribution after convolution, even though the intrinsic predicted gradients are monotonic (see, for example, their fig. 8 bottom-right panels).

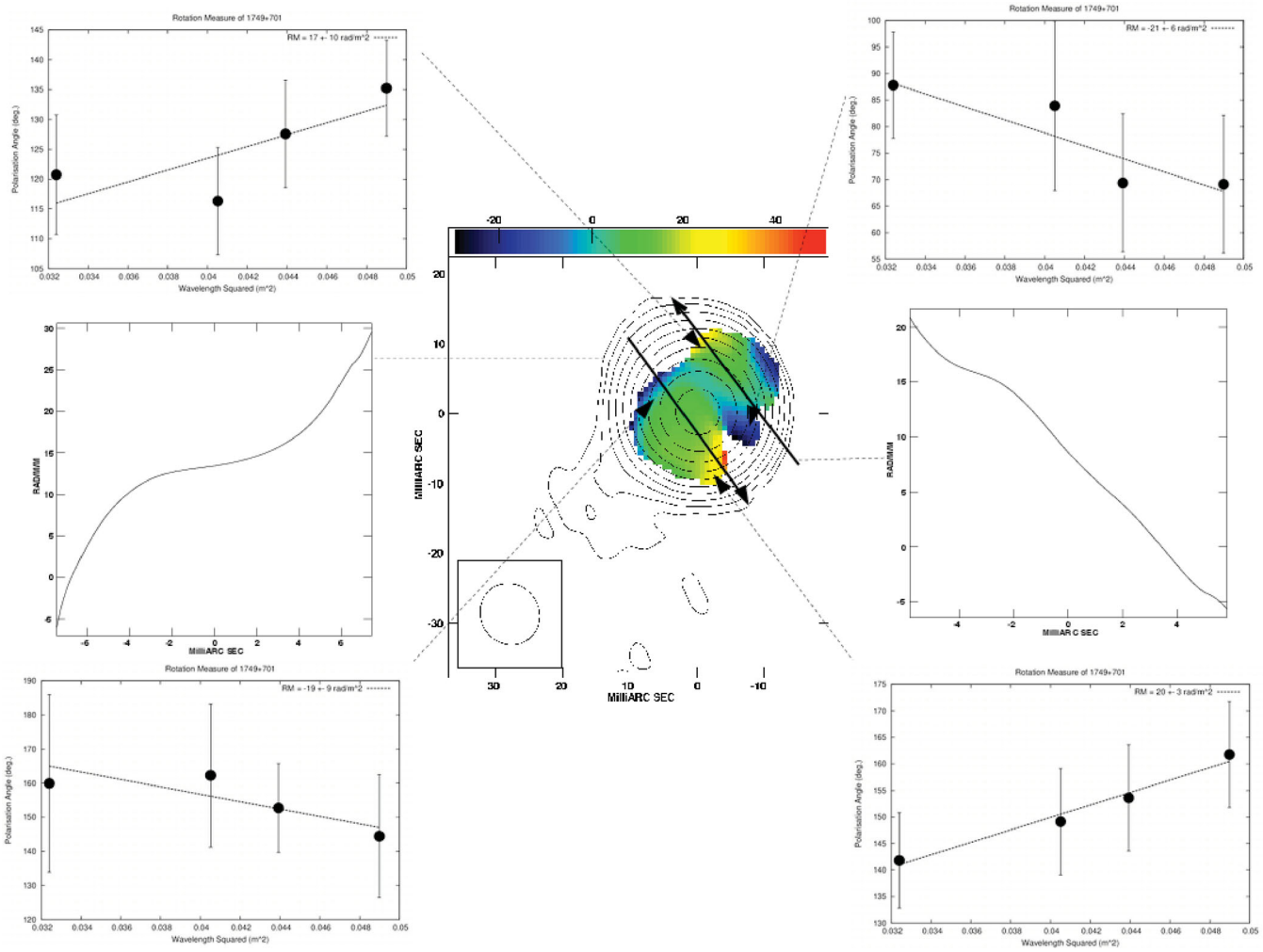

Figure 4. RM map of 1749+701 1.36–1.66 GHz. The accompanying panels show slices of the RM distribution across the core, and polarization angle (χ) versus wavelength-squared (λ^2) plots for pixels on either side of the core and jet. The errors shown are 1σ, and include the estimated random errors and the EVPA uncertainties added in quadrature. The peak of the I map is 0.6 Jy beam^{-1}; the bottom contour is 1.4 mJy beam^{-1} (2004 January). The beam used to construct the I and RM maps was 9.16 × 8.57 mas in position angle 49°.

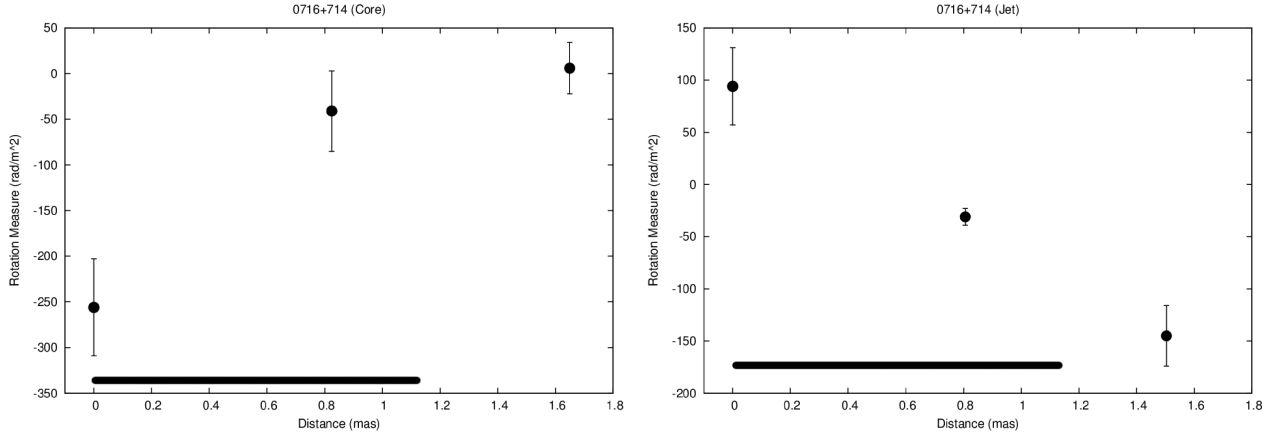

Figure 5. Plots of observed RM as a function of distance from a reference point on one side of the source structure across the core-region (left) and jet (right) RM distributions of 0716+714 at 4.6–15.4 GHz. The positions of each point and the corresponding RM values and their errors are listed in Table 2. The horizontal bar shows the approximate size of the beam FWHM.

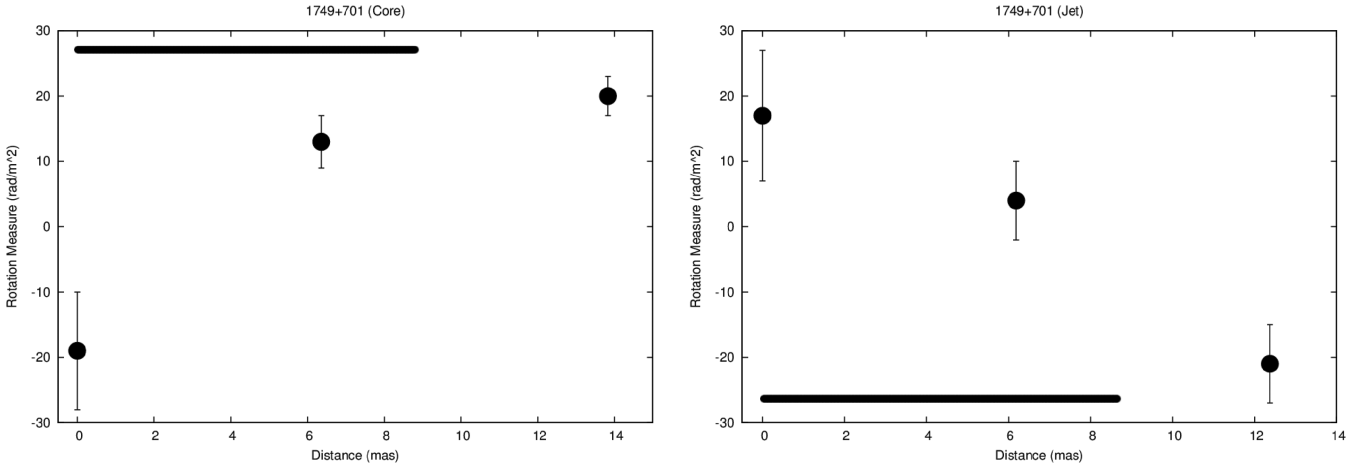

Figure 6. Plots of observed RM as a function of distance from a reference point on one side of the source structure across the core-region (left) and jet (right) RM distributions of 1749+701 at 1.36–1.67 GHz. The positions of each point and the corresponding RM values and their errors are listed in Table 2. The horizontal bar shows the approximate size of the beam FWHM.

The remaining criterion proposed by Taylor & Zavala (2010) is that the spectrum be optically thin at the location of the observed RM gradient. This criterion is motivated by two factors: (i) the desire to avoid possible jumps in the observed polarization angles due to optically thick–thin transitions with the observed frequency range and (ii) the fact that the fractional polarization can change rapidly with optical depth in the optically thick regime, leading to the possibility of wavelength-dependent polarization effects when regions having different optical depths at different frequencies are superposed, which could in principle lead to the fitting of spurious RM values in optically thick regions when these are inhomogeneous.

This criterion is clearly satisfied by the gradients across the jets of 0716+714 and 1749+701, which are all optically thin. The core regions of these two objects are also predominantly, but not fully, optically thin. The core-region spectral indices and χ values provide no evidence for a transition between optically thick and optically thin in the frequency ranges considered, consistent with the fact that the observed Faraday Rotations in the polarization angles are all no greater than a few tens of degrees. Thus, there is no reason to suspect that jumps in the observed polarization angles due to optical-depth transitions are contributing to the observed core-region RMs. We cannot completely rule out the possibility that the polarization angles in the core region are subject to wavelength-dependent optical-depth effects; however, we consider this to be unlikely, for two reasons: (i) the degrees of polarization in the core regions are $m_{\rm core} \simeq 3$–4 per cent for 0716+714 and $m_{\rm core} \simeq 7$ per cent for 1749+701, indicating a substantial contribution from optically thin regions and (ii) the quality of the λ^2 fits for the core regions is no worse than for the optically thin jet regions.

Thus, our detection of the RM gradients across the jets can be considered firm, while the detection of the oppositely directed RM gradients across the core may be somewhat more tentative, due to the small possibility that the observed polarization could be affected by optical-depth effects at some of the observed frequencies. This is much less likely to be the case for 1749+701, since the observed frequencies span the relatively narrow range from 1.36–1.67 GHz.

5.5 Reversal of RM gradients in the core region and jet

In both 0716+714 and 1749+701, the tentative transverse RM gradients detected in the core region are opposite in direction to the RM gradients detected across the jets (Figs 3–6). In fact, a similar behaviour is shown by the parsec-scale RM distribution for 3C 120 presented by Gómez et al. (2011): their RM map for 1999 January shows higher positive values on the southern side of the jet at the distance of components L and K (about 4 mas from the core), but more negative values on the southern side of the jet at the distance of component O (about 2 mas from the core).

At first, this seems difficult to understand, since the direction of an RM gradient associated with a helical $\boldsymbol{B}$ field is essentially determined by the direction of the rotation of the central accretion disc and the direction of the poloidal field it winds up, both of which we would expect to be constant in time. We can offer several possible explanations for this result. We briefly discuss these below and explain our reasoning for identifying the one that we think is the most likely (see also Mahmud et al. 2009).

Torsional oscillations of the jet: One possible interpretation of oppositely directed core and jet transverse RM gradients could be that the direction of the azimuthal $\boldsymbol{B}$-field component changed as a result of torsional oscillations of jet (Bisnovatyi-Kogan 2007). Such torsional oscillations, which may help stabilize the jets, could cause a flip of the azimuthal $\boldsymbol{B}$ field from time to time or equivalently with distance from the core, given the jet outflow. In this scenario, we expect that the direction of the observed transverse RM gradients may reverse from time to time when the direction of the torsional oscillation reverses; this reversal pattern would presumably then propagate outward with the jet.

Reversal of the 'pole' facing the Earth: Another possible interpretation could be that the 'pole' of the black hole facing the Earth reversed. One way to retain a transverse RM gradient in a helical magnetic field model but reverse the direction of this gradient, is if the direction of rotation of the central black hole (i.e. the direction in which the field threading the accretion disc is 'wound up') remains constant, but the 'pole' of the black hole facing the Earth changes from north to south, or vice versa. To our knowledge, it is currently not known whether such polarity reversals are possible for the central black hole of AGN or on what time-scale they could occur.

*Nested-helix **B**-field structure:* A simpler and more likely explanation is a magnetic-tower-type model, with poloidal magnetic flux and poloidal current concentrated around the central axis (Lynden-Bell 1996; Nakamura, Li & Li 2006). Fundamental physics dictates that the magnetic-field lines must close; in this picture, the magnetic field forms meridional loops that are anchored in the inner and outer parts of the accretion disc, which become twisted due to the differential rotation of the disc. This should essentially give rise to an 'inner' helical ***B*** field near the jet axis and an 'outer' helical field somewhat further from the jet axis. These two regions of helical field will be associated with oppositely directed RM gradients, and the total observed RM gradient will be determined by which region of helical field dominates the observed RMs. Thus, the presence of a change in the direction of the observed transverse RM gradient between the core/innermost jet and jet regions well resolved from the core could represent a transition from dominance of the inner to dominance of the outer helical ***B*** fields in the total observed RM. This seems to provide the simplest explanation for the RM-gradient reversals we observe in these two objects.

Typically, we would expect the direction of the RM gradients in the core and jet (i.e. the regions whose net RM is determined by the inner/outer helical fields) to remain constant in time, since they should be determined by the source geometry and viewing angle. Mahmud et al. (2009) discuss the possibility that this type of 'nested helical field' structure could also occasionally give rise to changes in the direction of the observed RM gradients with time within a given source.

6 CONCLUSION

The polarization RM images for the two BL Lac objects presented here provide new evidence in support of helical magnetic fields associated with the jets of these AGN, most importantly the presence of transverse RM gradients across the jets of both objects. There is also a dominance of transverse ***B*** fields in the jets of 0716+714 and 1749+701, and signs of 'spine-sheath' polarization structures or orthogonal polarization offset towards one side of the jet in both these sources, consistent with the possibility that these jets carry a helical magnetic-field component: this type of structure can also come about naturally in the case of a helical jet ***B*** field (e.g. Lyutikov et al. 2005; Pushkarev et al. 2005). We interpret the observed transverse RM gradients as being due to the systematic variation of the toroidal component of a helical ***B*** field across the jet (Blandford 1993). We note in this connection that the transverse RM gradients in both 0716+714 and 1749+701 have opposite signs on either side of the jet, making it impossible to explain the gradients as an effect of changing thermal electron density alone (there must be a change in the direction of the line-of-sight magnetic field).

We have also detected tentative transverse RM gradients in the region of the observed VLBI core in both BL Lac objects, which can be interpreted as being associated with helical ***B*** fields in the innermost jets of these sources. Furthermore, we have found a striking new feature of the RM distributions in these objects: a reversal in the direction of the transverse RM gradients. Similar reversals can be seen in the RM images for 3C 120 presented by Gómez et al. (2011). At first, this seems difficult to understand, since the direction of the RM gradient associated with a helical ***B*** field is essentially determined by the direction of the rotation of the central accretion disc and the direction of the poloidal field it winds up. We suggest that the most likely explanation for these reversals is that we are dealing with a 'nested helical field' structure such as that present in magnetic-tower models, in which poloidal field lines emerging from the inner accretion disc form meridional loops that close in the outer part of the disc, with both sides of the loops (which have oppositely directed poloidal field components) getting 'wound up' by the disc rotation.

Further observations and studies of the RM-gradient reversals observed in these objects can potentially provide key information about how the geometry of the magnetic fields in these AGN jets evolve, and may provide information on the jet dynamics and jet collimation. We are currently using a variety of multifrequency polarization VLBA data to search for additional candidates for AGN jets displaying RM gradients and RM-gradient reversals on both parsec and decaparsec scales.

ACKNOWLEDGEMENTS

The research for this publication was supported by a Research Frontiers Programme grant from Science Foundation Ireland and the Irish Research Council for Science Engineering and Technology (IRCSET). The National Radio Astronomy Observatory is operated by Associated Universities Inc. We thank R. Zavala for kindly providing the modified version of the AIPS 'RM' task used in this work. We are also grateful to the referee for his careful reading of the paper and thoughtful, competent and useful comments.

REFERENCES

Asada K., Inoue M., Uchida Y., Kameno S., Fujisawa K., Iguchi S., Mutoh M., 2002, PASJ, 54, L39
Asada K., Inoue M., Kameno S., Nagai H., 2008a, ApJ, 675, 79
Asada K., Inoue M., Nakamura M., Kameno S., Nagai H., 2008b, ApJ, 682, 798
Asada K., Nakamura M., Inoue M., Kameno S., Nagai H., 2010, ApJ, 720, 41
Attridge J. M., Roberts D. H., Wardle J. F. C., 1999, ApJ, 518, L87
Bisnovatyi-Kogan G. S., 2007, MNRAS, 376, 1, 457
Blandford R. D., 1993, in Burgarella D., Livio M., O'Dea C., eds, Astrophysical Jets. Cambridge Univ. Press, Cambridge, p. 15
Broderick A. E., McKinney J. C., 2010, ApJ, 725, 750
Croke S. M., Gabuzda D. C., 2008, MNRAS, 386, 619
Gabuzda D. C., Lisakov M. M., 2009, Astron. Rep., 53, 51
Gabuzda D. C., Pushkarev A. B., Cawthorne T. V., 2000, MNRAS, 319, 1109
Gabuzda D. C., Murray É., Cronin P. J., 2004, MNRAS, 351, L89
Gabuzda D. C., Vitrishchak V. M., Mahmud M., O' Sullivan S., 2008, MNRAS, 384, 1003
Gómez J. L., Roca-Sogorb M., Agudo I., Marscher A. P., Jorstad S. G., 2011, ApJ, 733, 11
Hallahan D. R., Gabuzda D. C., Proceedings of Science. Available at: http://pos.sissa.it//archive/conferences/072/029/IX%20EVN%20Symposium_029.pdf
Hovatta T., Lister M. L., Aller M. F., Aller H. D., Homan D. C., Kovalev Y. Y., Pushkarev A. B., Savolainen T., 2012, AJ, 144, 105
Kardashev et al., 2013, Astron. Rep., in press
Königl A., 1981, ApJ, 243, 700
Kovalev Yu., Pushkarev A., Lobanov A., Sokolovsky K., 2008, Proceedings of Science. Available at: http://pos.sissa.it//archive/conferences/072/007/IX%20EVN%20Symposium_007.pdf
Laing R., 1996, Hardee P. E., Bridle A. H., Zensus J. A., eds, ASP Conf. Ser. Vol. 100, Energy Transport in Radio Galaxies and Quasars. Astron. Soc. Pac., San Francisco, p. 241
Lovelace R. V. E., Li H., Koldoba A. V., Ustyugova G. V., Romanova M. M., 2002, ApJ, 572, 445
Lynden-Bell D., 1996, MNRAS, 279, 389
Lyutikov M., Pariev V. I., Gabuzda D. C., 2005, MNRAS, 360, 869

Mahmud M., Gabuzda D. C., Bezrukovs V., 2009, MNRAS, 400, 2
Meier D. L., Koide S., Uchida Y., 2001, Sci, 291, 84
Murphy E., Gabuzda D. C., 2012, J. Phys. Conf. Ser., 355, 012009
Nakamura M., Uchida Y., Hirose S., 2001, New Astron., 6, 61
Nakamura M., Li H., Li S., 2006, ApJ, 652, 1059
Pacholczyk A. G., 1970, Radio astrophysics: Nonthermal Processes in Galactic and Extragalactic Sources, Freeman & Co., San Francisco
Pushkarev A. B., 2001, Astron. Rep., 45, 667
Pushkarev A. B., Gabuzda D. C., Vetukhnovskaya Yu. N., Yakimov V. E., 2005, MNRAS, 356, 859
Roberts D. H., Wardle J. F. C., Brown L. F., 1994, ApJ, 427, 718
Taylor G. B., Zavala R., 2010, ApJ, 722, L183
Zavala R. T., Taylor G. B., 2005, ApJ, 626, L73

APPENDIX A: MONTE CARLO SIMULATIONS

We constructed a model source with a transverse RM gradient present across its jet and carried out Monte Carlo simulations based on this model source. The model source is cylindrical, with a falloff in intensity on either side of the cylinder axis, and along the axis of the cylinder from a specified point located near one end of the cylinder (see Fig. A1). The resulting appearance of the model emission region is broadly speaking 'core–jet-like'.

Model visibility data were generated for each of the six frequencies listed in Section 2.1 (4.6–15.4 GHz), including the effect of the transverse RM gradient in the Q and U visibility data, and these model visibility data were sampled at precisely the (u, v) points at which 0716+714 was observed at each of the frequencies. Random thermal noise and the effect of uncertainties in the EVPA calibration by up to 3° were added to the sampled model visibilities. The amount of thermal noise added was chosen to yield rms values in the simulated images that were comparable to those in our actual observations.

Stokes I, Q and U images were constructed from these visibilities in the Common Astronomy Software Applications (CASA) package, using the same beam as was used in the observations of 0716+714 presented here (1.28 mas × 1.06 mas in PA = −0.°84, where the dimensions given correspond to the FWHM of the beam along its major and minor axes). The polarization of the model was chosen to yield a degree of polarization in the lower half of the convolved model image (the 'core' region) of about 5 per cent and a degree of polarization in the upper half of the convolved model image of about 10 per cent – similar to the observed values for 0716+714. The Q and U images were then used to construct the corresponding polarization angle images at each frequency, which were, in turn, used to construct RM images in the usual way. Finally, Monte Carlo RM maps were constructed, based on 200 independent realizations of the thermal noise and EVPA calibration uncertainty. In each case, the RM values were output to the RM map only in pixels in with the RM uncertainty indicated by the fitting was less than 80 rad m^{-2}; this value was chosen so that no spurious pixels were written to the output RM maps for any of the 200 realizations of the RM distribution. Finally, an average RM map was derived by averaging together all 200 individual realizations of the RM distribution.

This procedure was carried out for a number of model sources, all with a length of 1 mas and with transverse widths of 0.50, 0.35, 0.20. 0.10 and 0.05 mas. A recent observation of 0716+714 with the RadioAstron space antenna and the European VLBI Network has measured the size of a feature in the 6.2 cm core region to be 0.07 mas (Kardashev et al. 2013), and our narrowest jet was designed to have a width somewhat smaller than this.

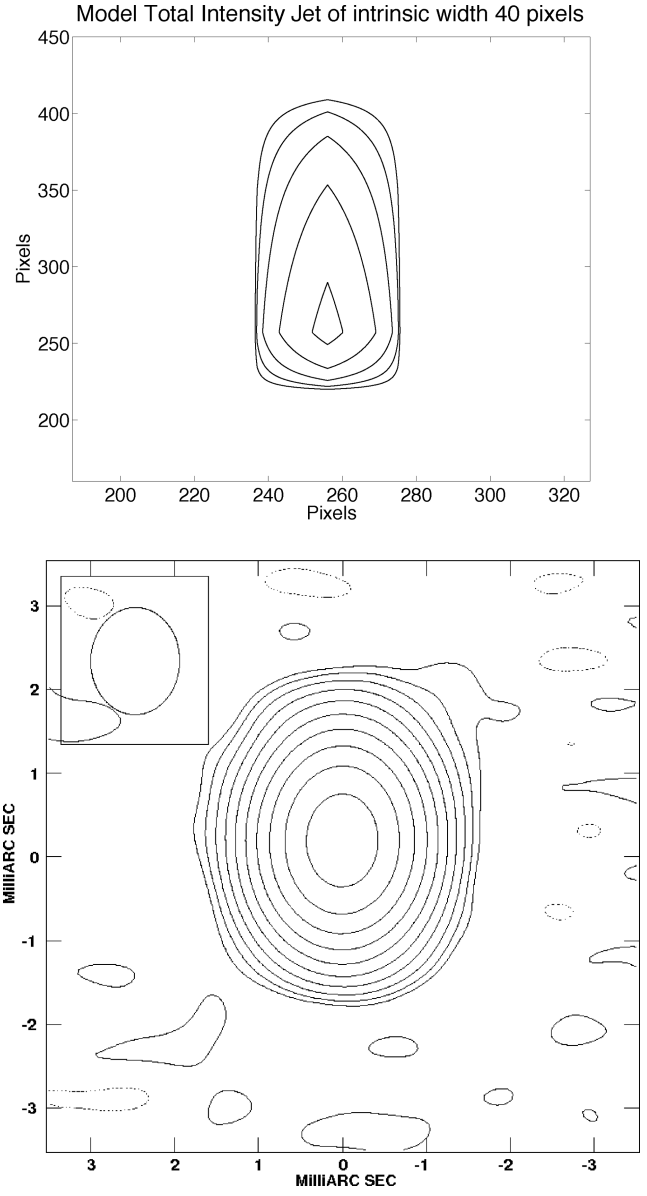

Figure A1. (Top) Intrinsic total intensity image of the model core–jet-like source with an intrinsic length of 1.0 mas (200 pixels) and an intrinsic width of 0.20 mas (40 pixels), used for the Monte Carlo simulations. (Bottom) One realization of a 'noisy' intensity map produced during the simulations. The convolving beam is 1.28 mas × 1.06 mas in PA = −0.°84 (shown in the upp left-hand corner of the convolved image). The peak of the unconvolved image is 5.62 × 10^{-4} Jy, and the contours are 5, 10, 20, 40 and 80 per cent of the peak. The peak of the convolved image is 1.11 Jy beam^{-1}, and the contours are −0.125, 0.125, 0.25, 0.5, 1, 2, 4, 8, 16, 32 and 64 per cent of the peak.

We considered two types of monotonic transverse RM gradients: unidirectional along the entire source structure, and oriented in one direction in the 'core' region and in the opposite direction in the 'jet' region, i.e. showing a reversal. These Monte Carlo simulations complement those carried out by Hovatta et al. (2012), in which simulated RM maps were made from model data that did not contain RM gradients, to determine the frequency of spurious transverse RM gradients appearing in the simulated RM maps.

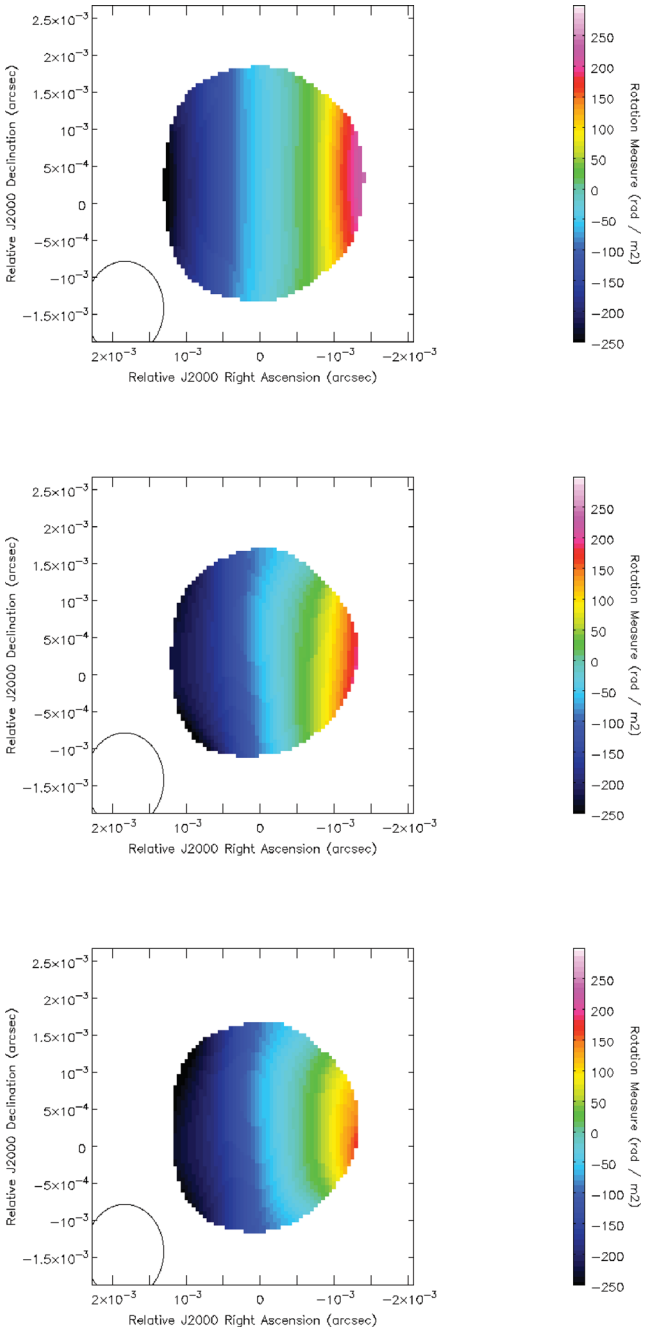

Figure A2. Results of Monte Carlo simulations using model core–jet sources with uniformly directed transverse RM gradients. The intrinsic width of the jet (RM gradient) is 0.35 mas. The convolving beam (1.28 mas × 1.06 mas in PA = −0.°84) is shown in the lower left-hand corner of each panel. The top panel shows the RM image obtained by processing the model data as usual, but without adding random noise or EVPA calibration uncertainty; pixels with RM uncertainties exceeding 10 rad m^{-2} were blanked. The remaining two panels show two examples of the 200 individual RM images obtained during the simulations; pixels with RM uncertainties exceeding 80 rad m^{-2} were blanked.

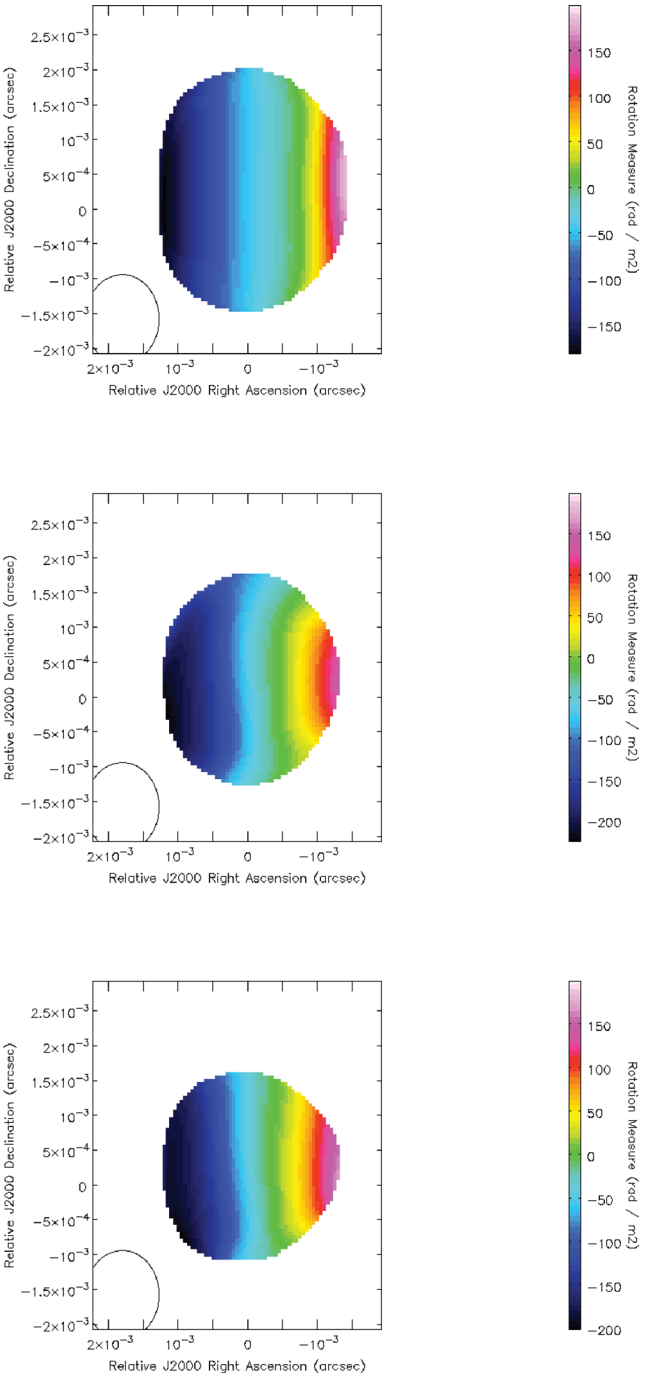

Figure A3. Same as Fig. A2 for a core–jet source with the same length but an intrinsic jet width of 0.20 mas.

One of the total intensity maps for the model source and an example of a 'noisy' realization of this map produced in the simulations are shown in Fig. A1 in this Appendix, and the results of the RM Monte Carlo simulations are shown in Figs A2–A9 in this Appendix (we do not show the results for the jet width of 0.50 mas, since these are very similar for the 0.35 mas jet width). The panels in Figs A2–A9 show (i) the RM map obtained by putting data without added thermal noise through the imaging procedure (i.e. the intrinsic RM distribution, but subject to errors due to the CLEAN process and limited *uv* coverage); (ii) two examples of the individual 'noisy' RM maps obtained. Note that the colour scales for the three maps in a corresponding set have been individually chosen to highlight the RM patterns present, and may differ somewhat in some cases.

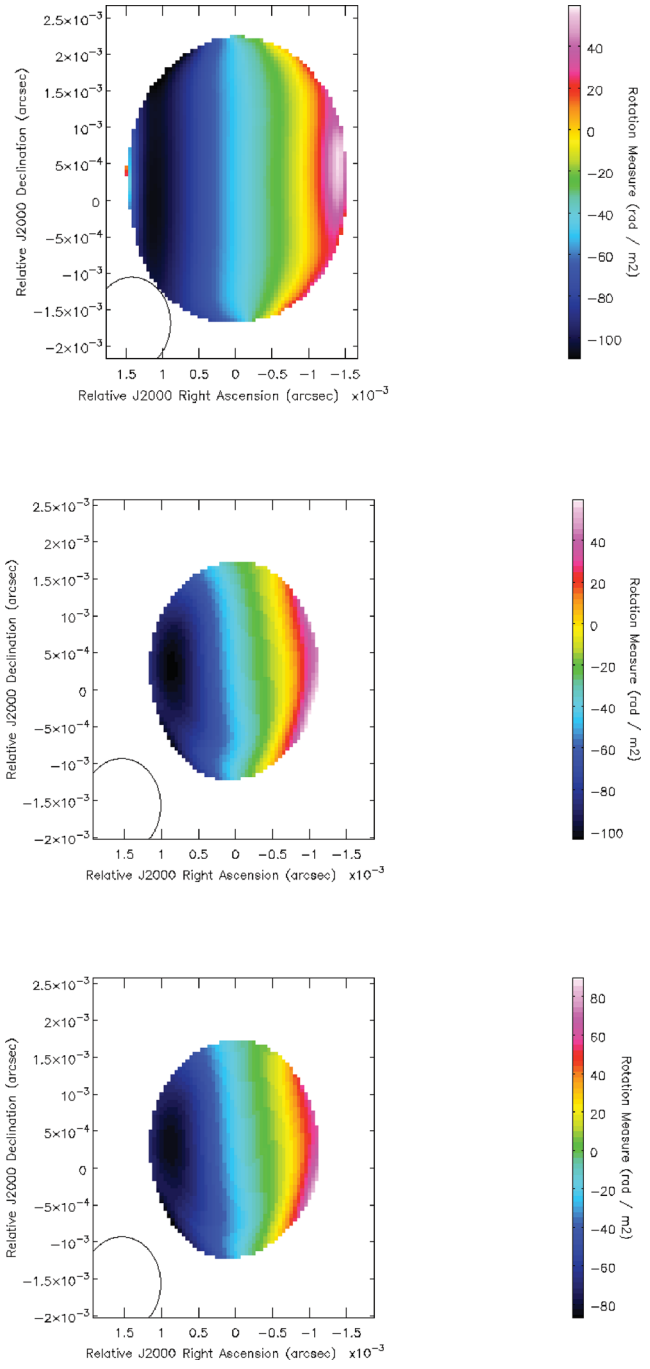

Figure A4. Same as Fig. A2 for a core–jet source with the same length but an intrinsic jet width of 0.10 mas.

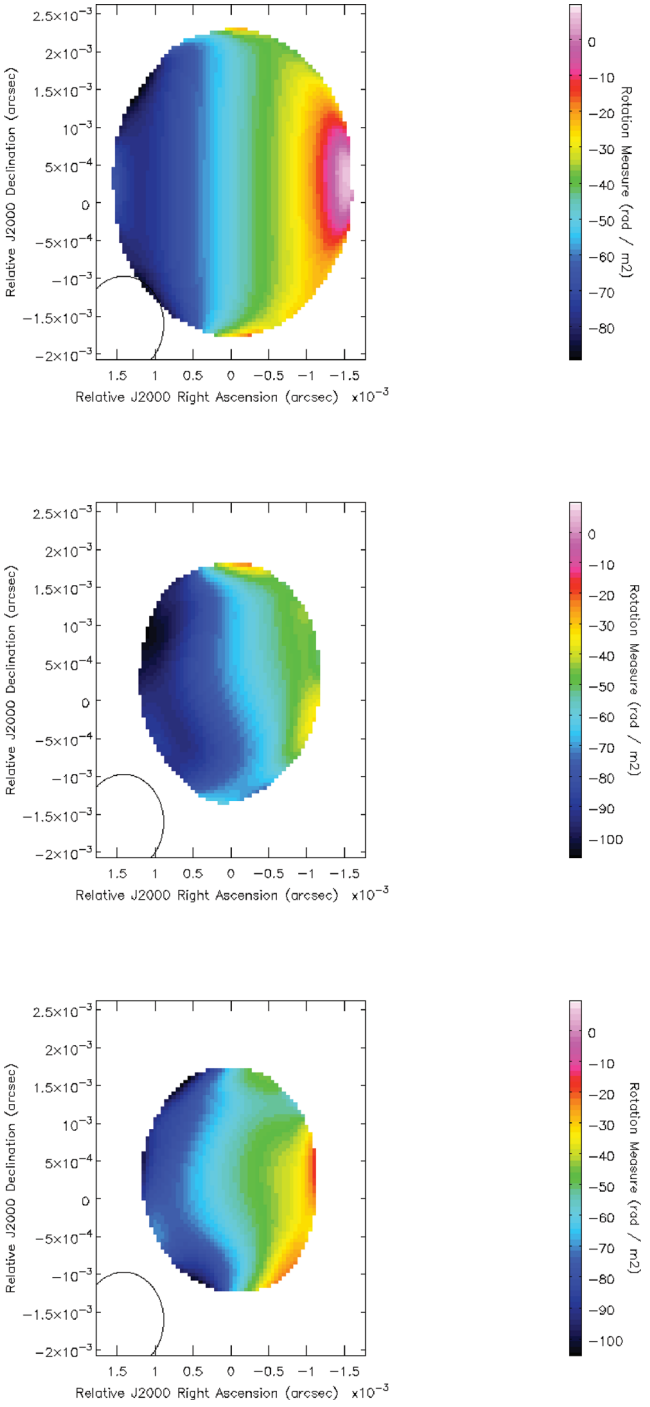

Figure A5. Same as Fig. A2 for a core–jet source with the same length but an intrinsic jet width of 0.05 mas.

In all cases, the RM gradients that were introduced into the simulated data are visible in the 'noisy' RM maps that were obtained, even when the intrinsic width of the jet is approximately 1/20 of the beam FWHM. This may seem surprising, but it is clearly demonstrated by the simulated data. The magnitude of the RM gradient is reduced by the convolution more and more as the size of the beam relative to the intrinsic size of the jet width increases, but the RM gradients that were initially introduced into the simulated data remain visible. In the case of jet widths much less than the beam FWHM, the appearance of individual realizations can sometimes be fairly strongly distorted by noise; however, in all cases, averaging together all the individual realizations confirms the presence of the RM gradients in the simulated images.

These results essentially indicate that it may not be necessary to impose a restriction on the width spanned by an observed RM gradient, *provided that the difference between the RM values observed at opposite ends of the gradient is at least 3σ*. This is consistent with the results of Murphy & Gabuzda (2012), who investigated the effect of resolution on transverse RM profiles. It is also consistent

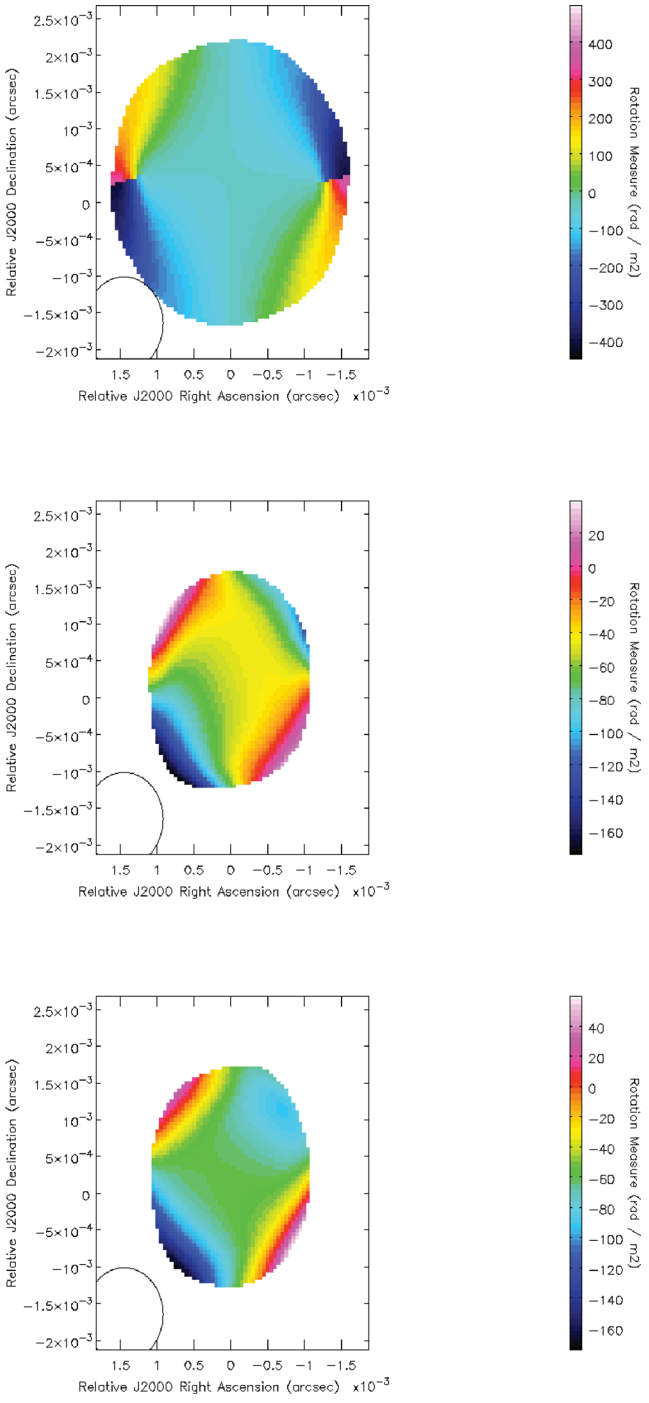

Figure A6. Results of Monte Carlo simulations using model core–jet sources with oppositely directed transverse RM gradients in the core region and inner jet. The intrinsic width of the jet (RM gradient) is 0.35 mas. The convolving beam (1.28 mas × 1.06 mas in PA = −0.°84) is shown in the lower left-hand corner of each panel. The top panel shows the RM image obtained by processing the model data as usual, but without adding random noise or EVPA calibration uncertainty; pixels with RM uncertainties exceeding 10 rad m^{-2} were blanked. The remaining two panels show two examples of the 200 individual RM images obtained during the simulations; pixels with RM uncertainties exceeding 80 rad m^{-2} were blanked.

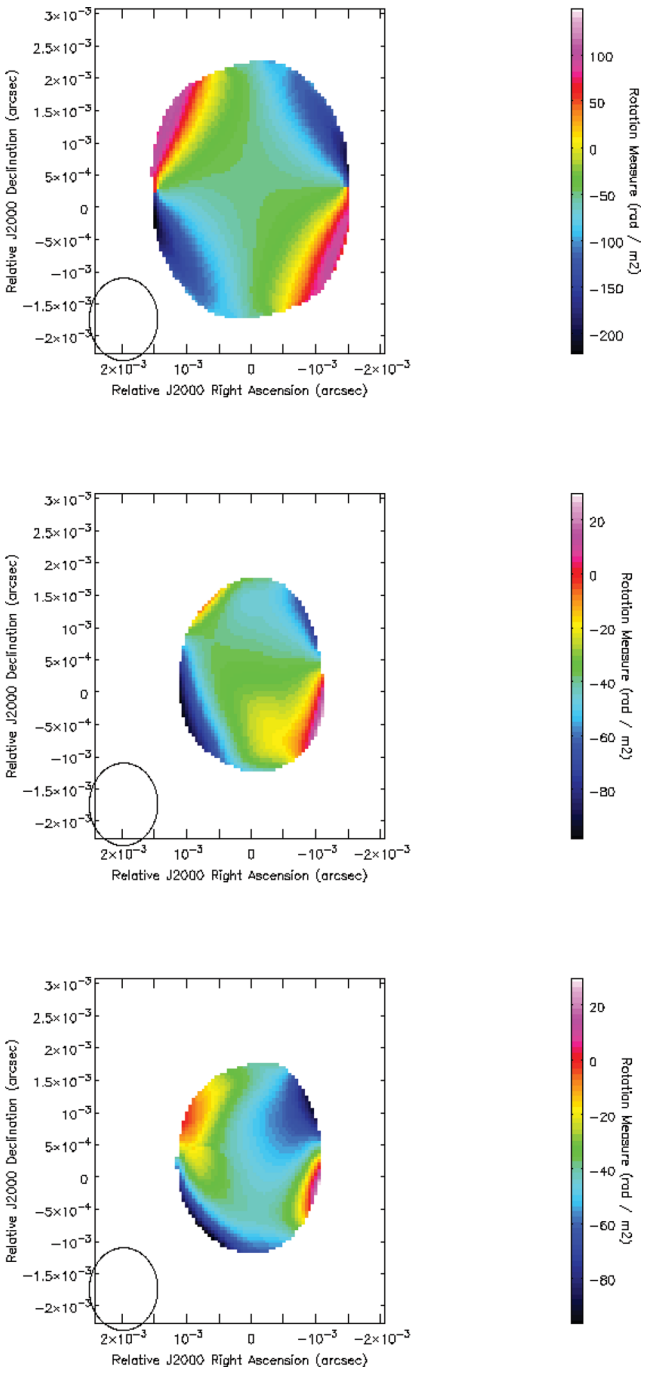

Figure A7. Same as Fig. A6 for a core–jet source with the same length but an intrinsic jet width of 0.20 mas.

with fig. 30 of Hovatta et al. (2012), which shows that the fraction of 'false positives', i.e. spurious RM gradients, that were obtained in their Monte Carlo simulations did not exceed $\simeq 1$ per cent when a 3σ criterion was imposed for the RM gradient, even when the observed width of the RM gradient was less than 1.5 beamwidths. It becomes important to place some restriction on the width spanned by the gradient if the difference between the RM values being compared is less than 3σ, as was also shown clearly by the Monte Carlo simulations of Hovatta et al. (2012).

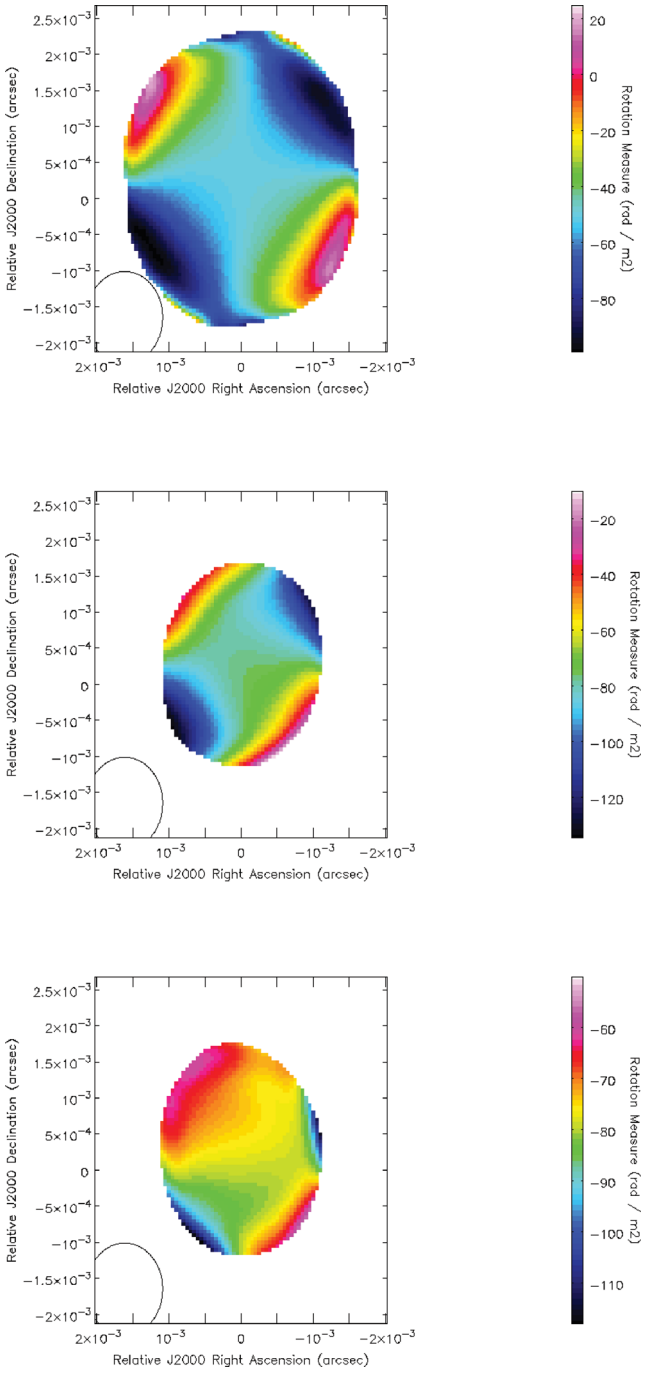

Figure A8. Same as Fig. A6 for a core–jet source with the same length but an intrinsic jet width of 0.10 mas.

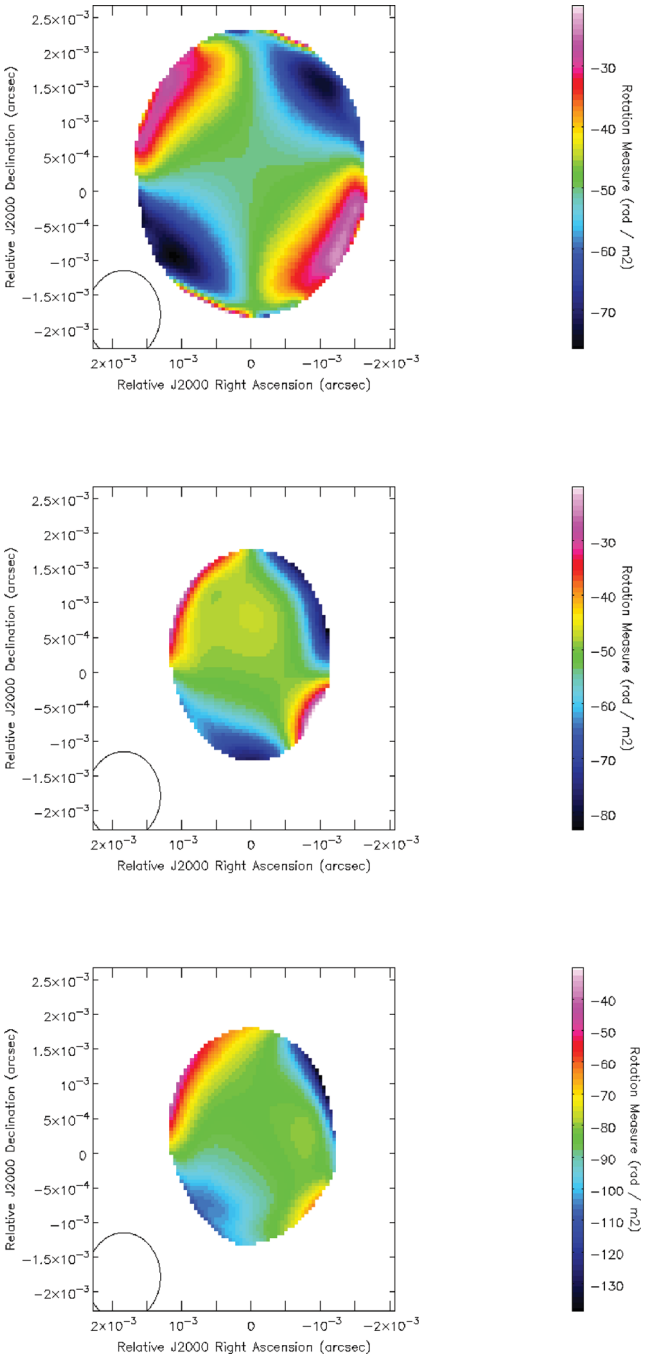

Figure A9. Same as Fig. A6 for a core–jet source with the same length but an intrinsic jet width of 0.05 mas.

This paper has been typeset from a TEX/LATEX file prepared by the author.